crystals

MDPI

Article

Nanocrystalline $(Cu_{0.5}Ni_{0.5})_yFe_{3-y}O_4$ Ferrites: Synthesis and Characterization

Nikolay Velinov [1,*], Tanya Petrova [1], Daniela Karashanova [2], Genoveva Atanasova [3] and Daniela Kovacheva [3]

[1] Institute of Catalysis, Bulgarian Academy of Sciences, 1113 Sofia, Bulgaria; silberbarren@abv.bg
[2] Institute of Optical Materials and Technologies, Bulgarian Academy of Sciences, 1113 Sofia, Bulgaria; dkarashanova@yahoo.com
[3] Institute of General and Inorganic Chemistry, Bulgarian Academy of Sciences, 1113 Sofia, Bulgaria; genoveva@svr.igic.bas.bg (G.A.); didka@svr.igic.bas.bg (D.K.)
* Correspondence: nikivelinov@ic.bas.bg

Abstract: Nanocrystalline materials with the composition of $(Cu_{0.5}Ni_{0.5})_yFe_{3-y}O_4$ and a spinel structure were synthesized by the auto-combustion sol–gel method. The materials were characterized by powder X-ray diffraction, Mössbauer spectroscopy, transmission electron microscopy, X-ray photoelectron spectroscopy, and N_2 physisorption. A decrease in the unit cell parameter and increase in the crystallite size with a decrease in the copper and nickel content in ferrites were evidenced. Mössbauer analysis determined that iron ions are in the 3+ states in all compositions. Transmission electron microscopy showed that synthesized ferrite materials consisted of nanoparticles with narrow size distributions. The catalytic properties of synthesized ferrites were studied in the reaction of ethyl acetate oxidation and methanol decomposition. The conversion of ethyl acetate and CO_2 selectivity increased with temperature, and this effect was most pronounced for $(Cu_{0.5}Ni_{0.5})_{0.5}Fe_{2.5}O_4$, for which the main part of the particles possessed sizes below 10 nm, and the mean diameter was calculated to be 4.3 nm. The catalytic activity in the reaction of methanol decomposition was the highest for $(Cu_{0.5}Ni_{0.5})_{0.25}Fe_{2.75}O_4$, and it decreased with the increase in Cu and Ni content in the samples. The analysis of the samples after the catalytic test indicated significant reduction transformations within the catalysts. Under the reaction medium, the spinel phase decomposed through the formation of Hägg carbide.

Keywords: ethyl acetate oxidation; methanol decomposition; Mössbauer spectroscopy; nanocrystalline spinel ferrite

Citation: Velinov, N.; Petrova, T.; Karashanova, D.; Atanasova, G.; Kovacheva, D. Nanocrystalline $(Cu_{0.5}Ni_{0.5})_yFe_{3-y}O_4$ Ferrites: Synthesis and Characterization. *Crystals* **2024**, *14*, 233. https://doi.org/10.3390/cryst14030233

Academic Editor: Zongyou Yin

Received: 21 February 2024
Revised: 23 February 2024
Accepted: 27 February 2024
Published: 28 February 2024

1. Introduction

Spinel ferrite materials have drawn the attention of the large research community because of their potential application in electronics [1–3], medicine [4–6], and catalysis [7–11]. Numerous studies of spinel ferrites have been motivated by the interest to investigate the relationship between their composition, structure, and functional properties as magnetic, optical, catalytic, etc. [12–15].

It is well known that the general formula of spinel ferrite materials can be written as follows: $(M_xFe_{1-x})[M_{1-x}Fe_{1+x}]O_4$, where M is a divalent ion, the metallic cations in ( ) occupy the tetrahedral A sites, and the metallic cations in [ ] occupy the octahedral B sites. According to the occupation of divalent and three-valent cations of tetrahedral and octahedral positions, normal, inverse, and partial inverse spinel structures exist. When all divalent cations occupy only tetrahedral sites, the spinel structure is called normal; when all divalent cations occupy octahedral sites, it is inverse; and when divalent cations are distributed in tetrahedral and octahedral sites, it is partially inverse.

The synthesis of spinel ferrite materials (including nanocrystalline) has been intensively studied in recent years [7]. If they are structurally well defined, the possibility to make a solid solution allows for varying precise compositions and the catalytic properties of

the material. The physical and chemical properties of nanomaterials are strongly dependent on the size, shape, and morphology of the nanoparticles inside [16]. The influence of the synthesis method on the modeling of the properties is fundamental; hence, the selection of the most appropriate method for obtaining an optimal composition for the catalysis properties, such as specific surface area, chemical composition of the surface of the material, morphology, porosity, crystal defects, etc., is of crucial importance.

One of the most well-known synthesis methods is solid-state thermal synthesis, also called ceramic synthesis [17]. This method is based on the co-heating of a previously well-homogenized mixture of starting substances (most often oxides) according to a regime and temperatures that allow the full interaction of the components of the mixture. The production technology requires a gradual increase in temperature and an application of high temperatures (over 1500–2100 K). In general, the method is unsuitable for the preparation of catalysts and nanomaterials due to the deteriorated dispersion characteristics of the final product.

The method of co-precipitation has been successfully applied for the synthesis of spinel ferrite catalysts [18–20]. The operating conditions determine the properties and composition of the final product: the pH of the medium during precipitation, the concentration of the starting solutions, the temperature during precipitation, the rate of precipitation, the time of ripening of the precipitate, and the washing and the conditions of the subsequent thermal treatment. The precipitation process begins by mixing the aqueous solutions of metal salts with a solution of NaOH, NH_4OH, or $(NH_4)_2CO_3$. As a result, an insoluble precipitate of metal hydroxide, oxyhydroxide, or carbonate (hydroxycarbonate) is obtained. The obtained precipitate is converted into individual or mixed metal oxides during the thermal treatment stage. Theoretically, all soluble salts can be used in the preparation of insoluble compounds, but in many cases, a particular salt is preferred. When obtaining precipitates, in which the anions of the starting salt are included, these anions or their products are poisons, and the use of sulfates and chlorides is not desirable. It is preferable to use nitrates, where the incorporated NO_3^- in the sludge can be removed in subsequent processes. The advantages of the co-precipitation method are the high degree of homogenization of the composition, obtaining a suitable dispersed structure, and the possibility of producing nanomaterials. A disadvantage is the large amount of polluted water released.

Solution combustion synthesis is another method appropriate for the synthesis of nanoscale materials [21]. Since this is a high-temperature method, thermodynamically stable phases can also be obtained. The properties of the resulting powder materials depend, to a large extent, on the process parameters, the type of fuel, the oxidizer-to-fuel ratio, etc. The main requirements for the type of fuel used are that it should be water soluble and should have a lower ignition temperature. In the solution combustion synthesis, salts of nitrates, carbonates, sulfates (as oxidizing agents), and reducing agents (fuels) are used. The most commonly used organic compounds as fuels are urea, glycine, citric acid, sucrose, etc. [22,23]. This synthesis method has several advantages compared to other methods in terms of simplicity, cost-effectiveness, energy saving, high productivity, purity, and homogeneity. Using this synthesis method, homogeneous powders, very fine crystalline powders, and multi-component oxide ceramic powders can be obtained without any intermediate decomposition or calcination.

The aim of the present work is to synthesize nanocrystalline spinel ferrites of the $(Cu_{0.5}Ni_{0.5})_yFe_{3-y}O_4$ type and to study their structural and catalytic characteristics. The catalytic behavior of the obtained materials is followed in two test reactions—methanol decomposition and ethyl acetate oxidation. Methanol decomposition was used as a catalytic activity test due to the growing interest in methanol as a renewable source for safely storing and transporting hydrogen, syngas, or methane [11,24,25]. On the other hand, ethyl acetate, a common ester compound and gaseous pollutant prevalent in many industrial processes is released into the atmosphere without any purification, and finding out a cheap and effective catalyst for its complete oxidation is a great challenge [26,27].

2. Materials and Methods

Samples with the nominal composition $(Cu_{0.5}Ni_{0.5})_yFe_{3-y}O_4$, where y = 0.25, 0.5, and 0.75, were synthesized using the auto-combustion sol–gel method [11], which is a variant of the solution combustion synthesis. Citric acid was used in quantities equal to the sum of the metal ions. In short, the experimental procedure was as follows: $Cu(NO_3)_2 \cdot 3H_2O$, $Ni(NO_3)_2 \cdot 6H_2O$, and $Fe(NO_3)_3 \cdot 9H_2O$ in the corresponding stoichiometric ratio was dissolved in distilled water at room temperature by stirring; citric acid was added to the solution, and stirring continued at 333 K; the auto-combustion process was performed by heating the samples in an oven at 423 K for two hours. The samples were further thermally treated at 573 K for two hours.

Powder X-ray diffraction (XRD) patterns were collected within the range of 15° to 80° 2θ on a Bruker D8 Advance diffractometer with Cu K_α radiation and LynxEye detector. Phase identification was performed using the ICDD-PDF2 database. The average crystallite size (D) and the lattice parameter (a) of the crystalline phases in the samples were determined based on the experimental XRD profiles by using the PowderCell-2.4 software and appropriate corrections for the instrumental broadening.

Room temperature (RT) and liquid nitrogen temperature (LNT) Mössbauer spectra were obtained using a WissEl (Wissenschaftliche Elektronik GmbH, Starnberg, Germany) electromechanical spectrometer working in a constant acceleration mode. A $^{57}Co/Rh$ source with activity ≅ 50 mCi and α-Fe standard were used. The experimentally obtained spectra were fitted using WinNormos-for-Igor6 ver. 6.0 software. The parameters of hyperfine interaction such as isomer shift (δ), quadrupole splitting (Δ), quadrupole shift (2ε), effective internal magnetic field (B_{hf}), line widths (Γ_{exp}), and relative weight (G) of the partial components in the spectra were determined.

The morphology and microstructure of the nanoparticles in the catalytic materials, as well as the phase composition of the samples, were followed by High-Resolution Transmission Electron Microscope (TEM) JEOL JEM 2100 (JEOL Ltd., Tokyo, Japan) at 200 kV accelerating voltage. The powder of each material was dispersed into ethanol and sonicated for 3 min. Afterward, a drop of dispersion was fixed on a standard Cu TEM grid covered with amorphous carbon, and it was dried for 24 h in a dust-free atmosphere under ambient conditions.

The surface composition and electronic structure of materials were investigated by X-ray photoelectron spectroscopy (XPS). The measurements were performed in a VGESCALAB II (VG Scientific, Manchester, UK) system using AlKα radiation with an energy of 1486.6 eV. The binding energies (BE) were determined with an accuracy of ±0.1 eV utilizing the C1s line at 285.0 eV (from an adventitious carbon) as a reference. The element concentrations were evaluated based on the integrated peak areas after a Shirley-type linear background subtraction using theoretical Scofield's photoionization cross-sections.

The texture characteristics were measured based on the Nitrogen adsorption/desorption isotherms obtained at 77 K using Quantachrome Instruments NOVA 1200e (Boynton Beach, FL, USA). Prior to the measurements, the samples were heated up to 200 °C for 2 h. The nitrogen adsorption–desorption isotherms were analyzed to evaluate the following parameters: the specific surface areas (S_{BET}) were determined based on the Brunauer, Emmett, and Teller (BET) equation, and the total pore volume (V_t) and average pore diameter (D_{av}) were estimated according to the Gurvich rule at a relative pressure close to 0.99. The pore size distribution was determined through the desorption branch of the isotherms using the Barrett–Joyner–Halenda (BJH) method.

Methanol decomposition tests were carried out in a continuous flow type of microreactor (55 mg of catalyst diluted with crushed glass (weight ratio of 1:3) at 1.57 kPa partial pressure of methanol and WHSV of 100 h^{-1}). Before the catalytic experiment, the samples were pre-treated in situ for 1 h at 373 K in argon. The dosing of methanol was performed by saturator, thermostated at 273 K using argon as a carrier gas. The experimental data were collected under a thermo-programmed regime of the heating rate of 2 K/min within the tem-

perature range of 423–770 K. On-line gas chromatographic analyses were conducted on an HP 5890 apparatus equipped with flame ionization (FID) and thermal conductivity (TCD) detectors on a PLOT Q column. The total oxidation of ethyl acetate was performed under a temperature-programmed regime within the range of 400–773 K in a flow of 1.21 mol % ethyl acetate in air with *WHSV* of 100 h^{-1}. The results were calculated using the method of absolute calibration based on the carbon-based material balance. The methanol conversion was calculated as $X = ((C_{ini} - C_{cur})/C_{ini}) \times 100$, where C_{ini} and C_{cur} were the initial and current detected amounts of methanol, respectively. The selectivity to the ith product from methanol conversion was calculated as $Y_i/X \times 100$, where Y_i was its yield determined by $C_i/C_{ini} \times 100$ (C_i was the amount of ith product). The samples after the catalytic test in the reaction of ethyl acetate oxidation and the reaction of methanol decomposition were designated as $(Cu_{0.5}Ni_{0.5})_yFe_{3-y}O_4$-EA and $(Cu_{0.5}Ni_{0.5})_yFe_{3-y}$O-MD, respectively.

3. Results and Discussion

The XRD patterns of the synthesized samples are given in Figure 1. All diffraction peaks were assigned to cubic spinel phase S.G.: Fd-3m, No. 227. No additional peaks of secondary phases were found. The calculated unit cell parameters and average crystallite size are summarized in Table 1. It is evident that the crystallite size increases from about 8.5 nm to 10.2 nm with a decrease in copper and nickel content in the composition. It also established a decrease in unit cell parameter with the decrease in copper and nickel content in the ferrite composition, which could be explained by the smaller ionic radius of Fe^{3+} compared to Cu^{2+} and Ni^{2+}.

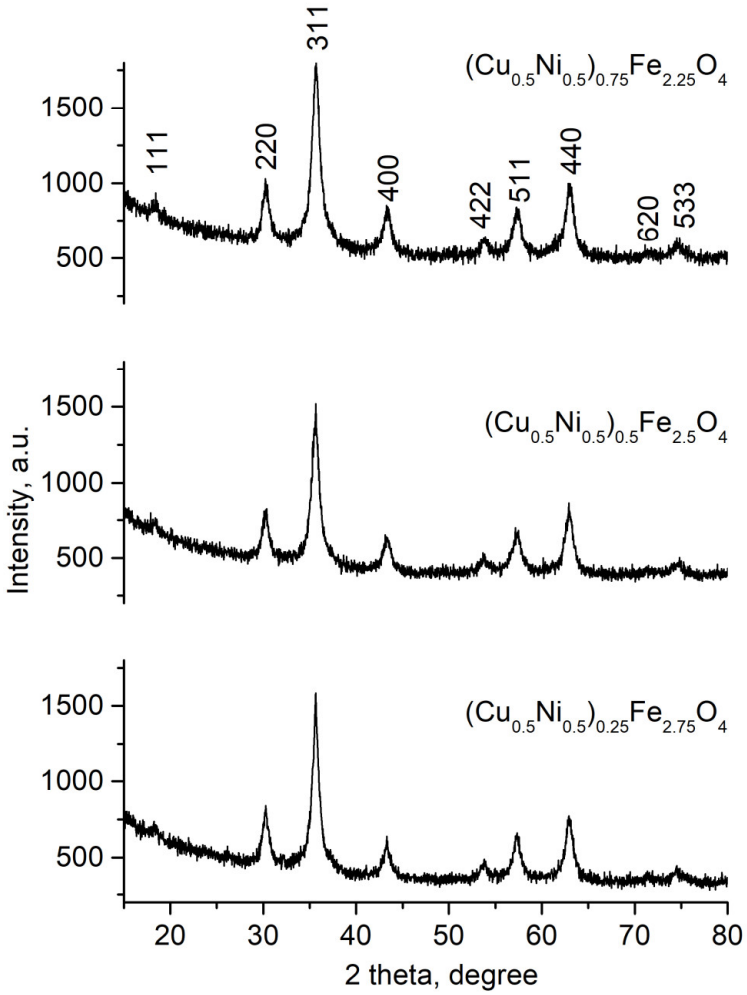

Figure 1. XRD patterns of the investigated samples.

Table 1. Average crystallite size (D) and lattice parameter (a) of the crystalline phases in samples determined based on the experimental XRD profiles.

Sample	Phase	D, nm	a, Å
$(Cu_{0.5}Ni_{0.5})_{0.75}Fe_{2.25}O_4$	spinel	8.52	8.3534
$(Cu_{0.5}Ni_{0.5})_{0.5}Fe_{2.5}O_4$	spinel	8.83	8.3478
$(Cu_{0.5}Ni_{0.5})_{0.25}Fe_{2.75}O_4$	spinel	10.18	8.3436

The Mössbauer spectra of the prepared materials were recorded at room temperature and LNT, and they are represented in Figure 2.

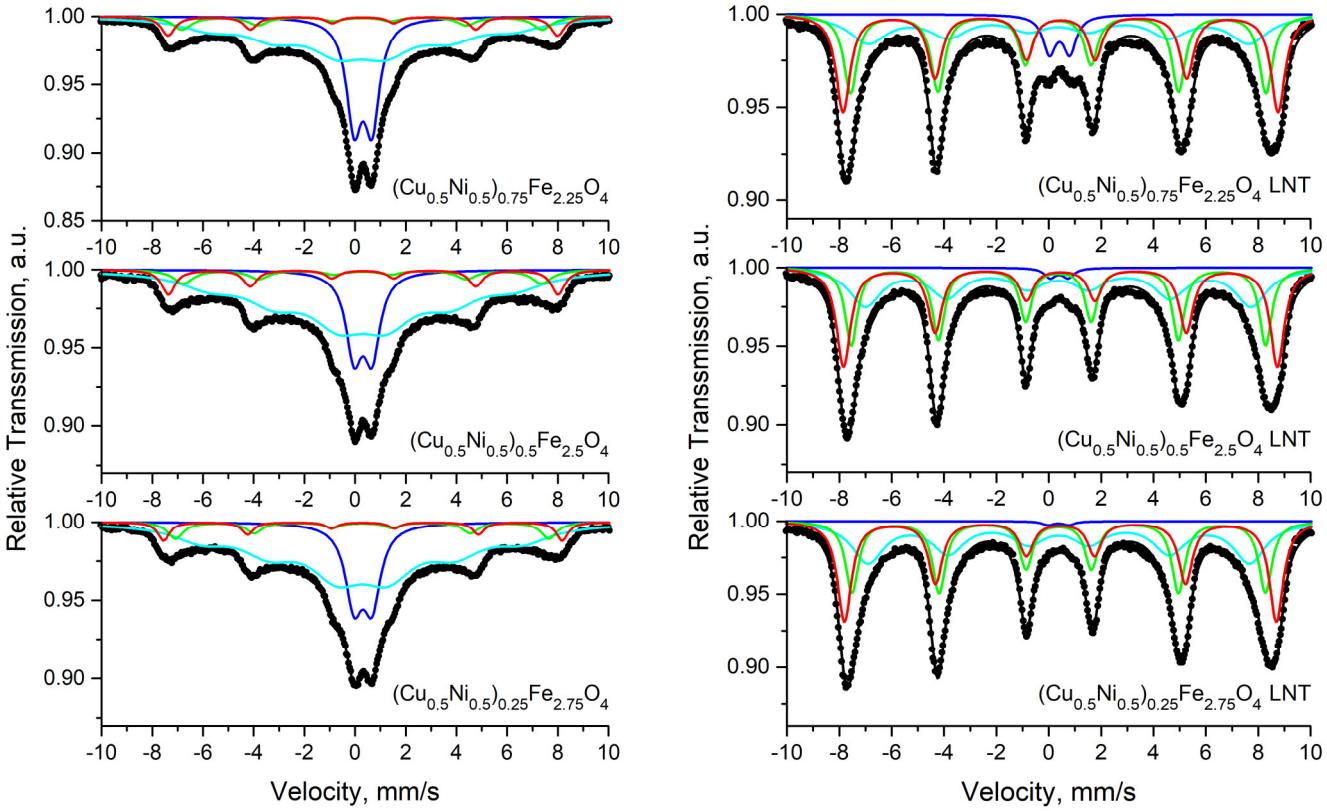

(**a**) (**b**)

Figure 2. Mössbauer spectra of the synthesized samples at room temperature and (**a**) and liquid nitrogen temperature (**b**).

The room temperature spectra of all samples consisted of doublet and sextets with wide lines. The best fit was obtained using a model with three sextets and one doublet. The calculated Mössbauer parameters in the result of fitting are represented in Table 2. It should be noted that there is no spectral component with parameters indicating the presence of iron 2+ in the samples. Therefore, the cation distribution in the spinel structure of the samples is expected to be like Fe^{2+}-deficient magnetite. The maghemite has a structure that can be considered as Fe^{2+}-deficient magnetite with the following formula:

$$(Fe_8^{3+})_A[Fe_{\frac{40}{3}}^{3+}\square_{\frac{8}{3}}]_BO_{32}, \quad (1)$$

where □ represents a vacancy, and A and B are tetrahedral octahedral positions, respectively [28].

Table 2. Mössbauer parameters of the synthesized samples at room temperature and at liquid nitrogen temperature (LNT).

Sample	Components	δ, mm/s	Δ (2ε), mm/s	B_{hf}, T	Γ_{exp}, mm/s	G, %
$(Cu_{0.5}Ni_{0.5})_{0.75}Fe_{2.25}O_4$	Sx1-$Fe^{3+}{}_{octa}$	0.31	−0.01	47.6	0.65	9
	Sx2-$Fe^{3+}{}_{tetra}$	0.28	0.00	44.1	0.91	9
	Sx3-Fe^{3+}	0.26	0.00	37.2	2.65	55
	Db-Fe^{3+}	0.31	0.71	-	0.73	27
$(Cu_{0.5}Ni_{0.5})_{0.5}Fe_{2.5}O_4$	Sx1-$Fe^{3+}{}_{octa}$	0.32	0.01	47.7	0.65	10
	Sx2-$Fe^{3+}{}_{tetra}$	0.29	0.00	43.8	0.95	8
	Sx3-Fe^{3+}	0.29	0.00	37.3	2.73	64
	Db-Fe^{3+}	0.31	0.71	-	0.78	18
$(Cu_{0.5}Ni_{0.5})_{0.25}Fe_{2.75}O_4$	Sx1-$Fe^{3+}{}_{octa}$	0.31	−0.01	48.8	0.56	6
	Sx2-$Fe^{3+}{}_{tetra}$	0.28	0.00	45.7	0.76	8
	Sx3-Fe^{3+}	0.29	0.00	39.3	2.65	67
	Db-Fe^{3+}	0.31	0.71	-	0.83	19
$(Cu_{0.5}Ni_{0.5})_{0.75}Fe_{2.25}O_4$ LNT	Sx1-$Fe^{3+}{}_{octa}$	0.45	−0.01	51.5	0.65	34
	Sx2-$Fe^{3+}{}_{tetra}$	0.36	0.00	49.2	0.62	32
	Sx3-Fe^{3+}	0.37	0.00	45.1	1.78	28
	Db-Fe^{3+}	0.41	0.78	-	0.6	6
$(Cu_{0.5}Ni_{0.5})_{0.5}Fe_{2.5}O_4$ LNT	Sx1-$Fe^{3+}{}_{octa}$	0.45	−0.01	51.4	0.65	34
	Sx2-$Fe^{3+}{}_{tetra}$	0.37	0.00	49.1	0.59	31
	Sx3-Fe^{3+}	0.36	0.00	45.7	1.47	33
	Db-Fe^{3+}	0.40	0.69	-	0.54	2
$(Cu_{0.5}Ni_{0.5})_{0.25}Fe_{2.75}O_4$ LNT	Sx1-$Fe^{3+}{}_{octa}$	0.44	0.00	51.2	0.65	33
	Sx2-$Fe^{3+}{}_{tetra}$	0.38	0.00	49.0	0.61	30
	Sx3-Fe^{3+}	0.38	0.00	45.2	1.50	36
	Db-Fe^{3+}	0.36	0.79	-	0.54	1

If the same principle of octahedral vacancy formation as in maghemite is accepted, and it is supposed for fully inverse spinel structure, the cation distribution in studied compositions should be as follows:

$$M_{0.25}Fe_{2.75}O_4 \ : \ (Fe_8^{3+})_A[Fe^{3+}_{\frac{280}{23}}M^{2+}_{\frac{40}{23}}\square_{\frac{48}{23}}]_BO_{32} \quad (2)$$

$$M_{0.5}Fe_{2.5}O_4 \ : \ (Fe_8^{3+})_A[Fe^{3+}_{\frac{120}{11}}M^{2+}_{\frac{40}{11}}\square_{\frac{16}{11}}]_BO_{32} \quad (3)$$

$$M_{0.75}Fe_{2.25}O_4 \ : \ (Fe_8^{3+})_A[Fe^{3+}_{\frac{200}{21}}M^{2+}_{\frac{120}{21}}\square_{\frac{16}{21}}]_BO_{32} \quad (4)$$

where M = Cu, Ni; □ represents a vacancy; A and B are tetrahedral octahedral positions, respectively.

As seen in Table 2, the first sextet named Sx1 has a higher isomer shift and higher magnetic field than the sextet Sx2, and it was attributed to iron 3+ ions in octahedral coordination. The Sx2 was assigned to tetrahedrally coordinated Fe^{3+}. The spectral areas of Sx1 and Sx2 in all the samples are nearly equal. This could be a sign that the largest ferrite particles have inverse spinel structures, i.e., Cu^{2+} and Ni^{2+} occupy octahedral positions in the spinel structure. The presence of a doublet and sextet with very wide lines (Sx3) is evidence for the presence of small particles which exhibit superparamagnetic behavior at room temperature in all samples [29]. The relative weight of the doublet in the $(Cu_{0.5}Ni_{0.5})_{0.75}Fe_{2.25}O_4$ sample is higher than that in the other samples (Table 2), which indicates a higher part of the lowest-size particles. This was confirmed by Mössbauer spectra of samples measured at LNT (Figure 2b, Table 2). It can be seen that the doublet part of spectra varies from 1% to 6%. It is observed to be dependent on the chemical composition of

samples. It can be concluded that the sample with a higher content of copper and nickel has a higher part of superparamagnetic doublet in the spectrum and lower crystallite size in the sample. Comparing the relative weight of Sx1 and Sx2 in LNT spectra, we observed a slight prevalence of the octahedral over tetrahedrally coordinated iron (Table 2). This indicates that the largest particles, which have magnetically ordered structures at LNT, have cation distribution similar to those described in the Equations (2)–(4). Unfortunately, it is difficult to determine the exact iron distribution in all particles in the samples because even at LNT, there exist significant numbers of subcritical size particles that exhibit superparamagnetic properties.

In order to study the morphology of the synthesized samples, as well as to obtain more detailed structural information, TEM analysis of the sample $(Cu_{0.5}Ni_{0.5})_{0.5}Fe_{2.5}O_4$ was performed (Figure 3). As seen, the material consists of nanoparticles with a narrow size distribution. The main part of the particles has a size below 10 nm, and the mean diameter was calculated to be 4.3 nm. The electron diffraction pattern was best matched and indexed with cubic spinel $CuFe_2O_4$ (S.G.: Fd-3m, No. 227, a = 8.36900 Å, COD Entry #96-591-0029), which confirms the results of the XRD analysis. In HRTEM images, the interplanar distances d = 2.52 Å and d = 2.09 Å corresponding to crystal planes (311) and (400) of cubic spinel $CuFe_2O_4$, respectively, were visualized in accordance with the SAED and XRD results.

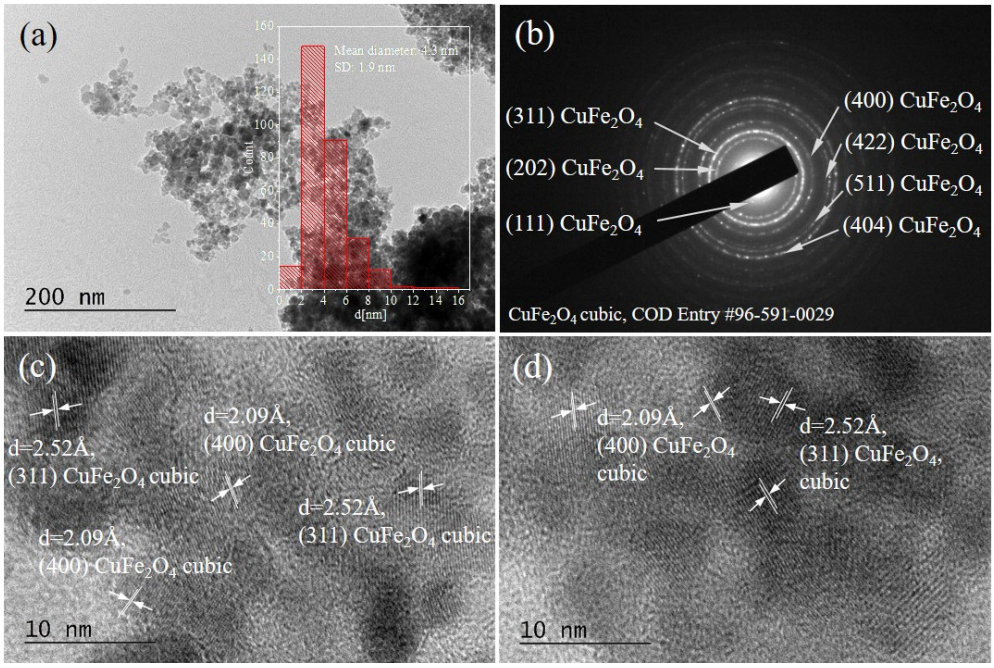

Figure 3. Bright Field TEM (BFTEM) micrograph and the particles size distribution histogram (**a**), the corresponding SAED pattern (**b**), and HRTEM micrographs (**c**,**d**) of $(Cu_{0.5}Ni_{0.5})_{0.5}Fe_{2.5}O_4$ catalytic material.

The electronic state and surface composition of synthesized materials were investigated by X-ray photoelectron spectroscopy. The high-resolution $Cu2p_{3/2}$, CuLMM, $Ni2p_{3/2}$, Fe2p, Fe3p, and O1s spectra are represented in Figure 4. Table 3 represents the data from the calculated surface concentration of the elements of the samples. The core-level $Cu2p_{3/2}$ spectra (Figure 4a) demonstrate the main peak centered at 933.5 eV and shake-up peaks at 940–945 eV. The copper LMM Auger lines (Figure 4b) are also recorded. The binding energy of the $Cu2p_{3/2}$ core level, the kinetic energy of the CuLMM Auger lines (917.6 eV), and the presence of a satellite at 940–945 eV in all the samples is characteristic of the presence of copper ions mainly in the 2+ oxidation state. [30]. The $Ni2p_{3/2}$ peak (Figure 4c) with a binding energy of 854.8 eV is characteristic of Ni^{2+} [31]. The binding energies of $Fe2p_{3/2}$,

$Fe2p_{1/2}$, (Figure 4d), and Fe3p (Figure 4e) thus obtained are 710.8 eV, 724.4 eV, and 55.6 eV, respectively. The binding energy of the Fe2p and Fe3p, spin-orbit splitting of 13.6 eV, as well as the presence of the satellite peak at about 719 eV correspond well to the binding energies and shape of the spectra of Fe^{3+} in Fe_2O_3 [32]. The maximum of the O1s peak (529.8 eV, Figure 4f) corresponds to lattice oxygen in metal oxides according to [33]. No other elements, including nitrogen, were detected.

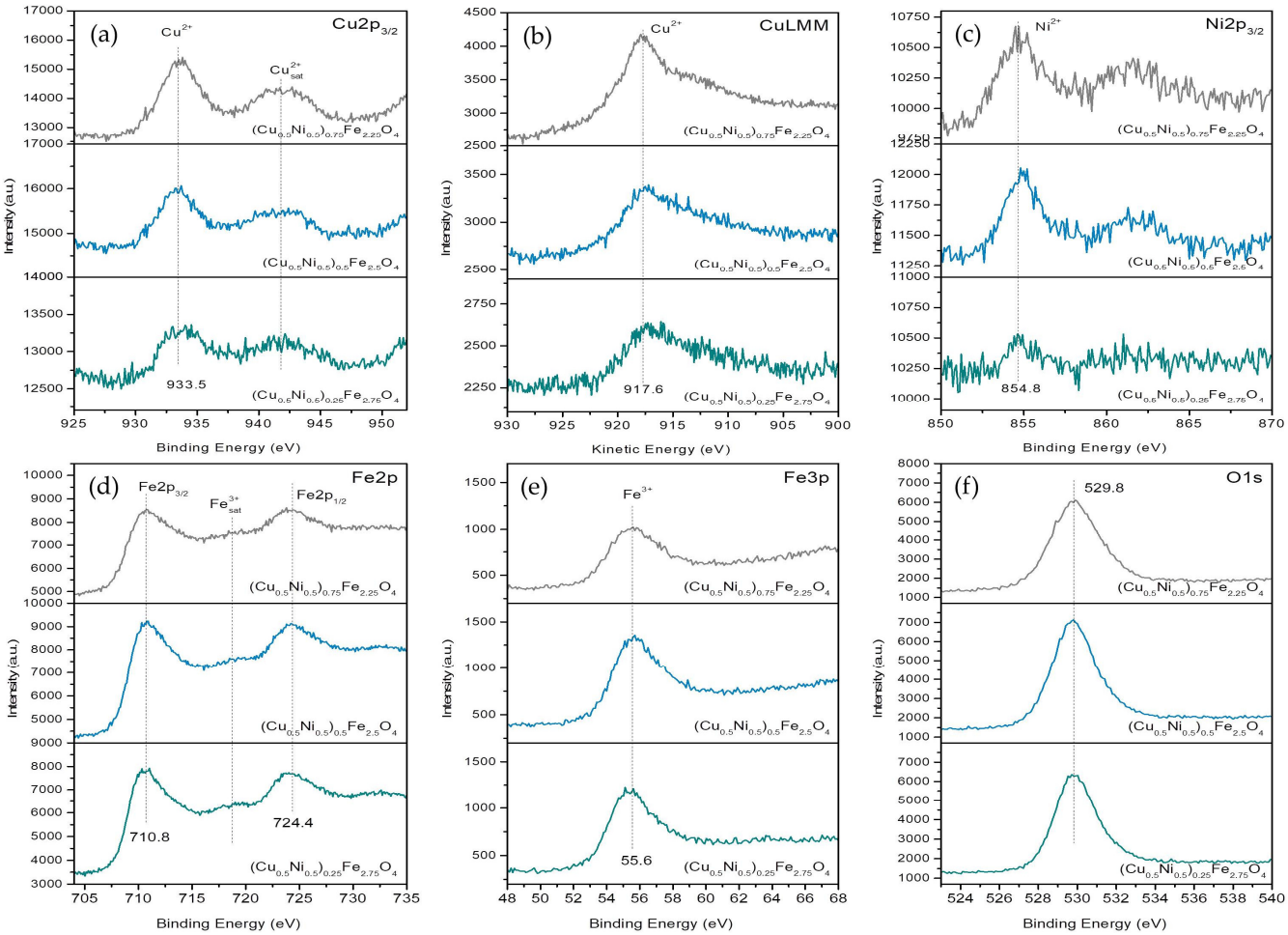

Figure 4. Partial XPS spectra of: $Cu2P_{3/2}$ (**a**), CuLMM (**b**), $Ni2p_{3/2}$ (**c**), Fe2p (**d**), Fe3p (**e**), and O1s (**f**) of the investigated samples.

Table 3. Surface (XPS) chemical compositions of the samples.

Sample	O, at. %	Cu, at. %	Fe, at. %	Ni, at. %
$(Cu_{0.5}Ni_{0.5})_{0.75}Fe_{2.25}O_4$	68.5	14.3	13.7	3.5
$(Cu_{0.5}Ni_{0.5})_{0.5}Fe_{2.5}O_4$	73.7	6.5	17.1	2.7
$(Cu_{0.5}Ni_{0.5})_{0.25}Fe_{2.75}O_4$	75.2	4.5	19.0	1.3

The nitrogen physisorption results are presented in Figure 5 and Table 4. All the samples displayed type IV isotherms with a hysteresis loop of Type H1, according to the IUPAC classification. This type of isotherm is characteristic of mesoporous materials. A type H1 hysteresis loop is inherent for materials that have nearly identical spheres, which are arranged into a comparatively ordered array, and have narrow pore size distributions [34,35]. This is also evident from the pore size distribution, obtained by the BJH method, which proves the presence of mesoporous structure. The values of the average diameter and volume of the pores (Table 4) confirm the results obtained from the BET analysis. It can

be stated that the relatively high specific surface areas of the obtained spinel ferrites make them suitable to function as catalysts.

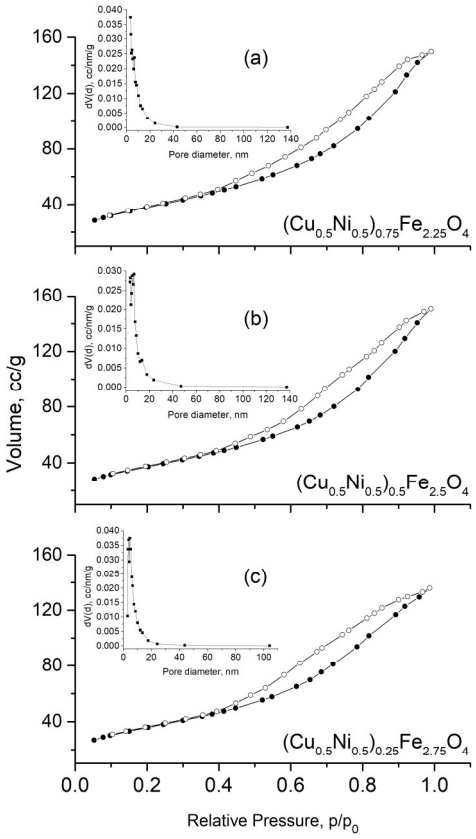

Figure 5. Nitrogen adsorption-desorption isotherms and pore size distributions for samples $(Cu_{0.5}Ni_{0.5})_{0.75}Fe_{2.25}O_4$ (**a**), $(Cu_{0.5}Ni_{0.5})_{0.5}Fe_{2.5}O_4$ (**b**), and $(Cu_{0.5}Ni_{0.5})_{0.25}Fe_{2.75}O_4$ (**c**).

Table 4. Nitrogen physisorption data: specific surface area (S_{BET}), total pore volume (V_t), average pore diameter (D_{av}).

Sample	S_{BET} [m^2/g]	V_t [cm^3/g]	D_{av} [nm]
$(Cu_{0.5}Ni_{0.5})_{0.75}Fe_{2.25}O_4$	136	0.28	6.8
$(Cu_{0.5}Ni_{0.5})_{0.5}Fe_{2.5}O_4$	133	0.23	7.0
$(Cu_{0.5}Ni_{0.5})_{0.25}Fe_{2.75}O_4$	128	0.21	6.6

The oxidation of EA was observed to be above 550–600 K (Figure 6). The main product of the oxidation was CO_2. At 50% conversion, only about 5–6% acetaldehyde, 1–4% ethanol, and 3% C_2H_4 were detected as by-products. The conversion and the CO_2 selectivity increased with temperature, and this effect was most pronounced for $(Cu_{0.5}Ni_{0.5})_{0.5}Fe_{2.5}O_4$. The smoother shape of the conversion curves above 620–630 K indicates a loss of catalytic activity.

The Mössbauer spectra of samples after the reaction of ethyl acetate oxidation are represented in Figure 7a. The calculated parameters are given in Table 5. As seen, the Mössbauer spectra before and after the catalytic test consist of the same components. We observed a significant decrease in the area of superparamagnetic doublets in all tested samples. This could be due to particle size increasing as a result of heating up to 700 K during catalytic testing. TEM analysis of the sample $(Cu_{0.5}Ni_{0.5})_{0.5}Fe_{2.5}O_4$-EA (Figure 8) confirms the preservation of the cubic spinel structure after the catalytic activity test for ethyl acetate. Moreover, TEM proves the recrystallization of ferrite particles as the mean diameter was calculated to increase from 4.3 Å to 6.5 Å after the test.

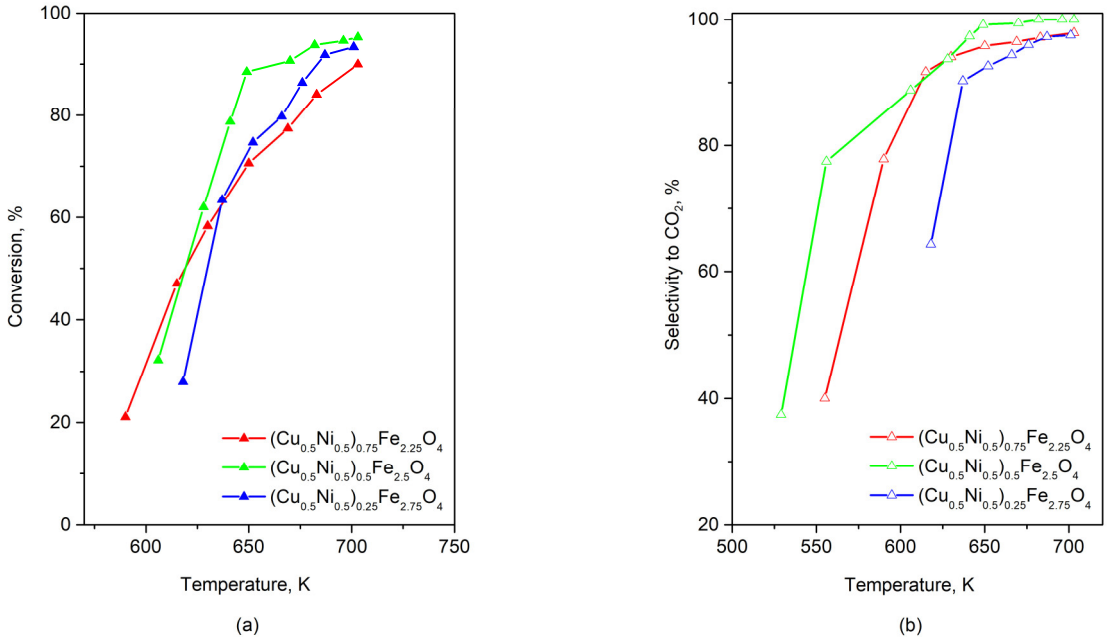

Figure 6. Conversion (**a**) and selectivity to CO_2 (**b**) vs. temperature in total oxidation of ethyl acetate for various samples.

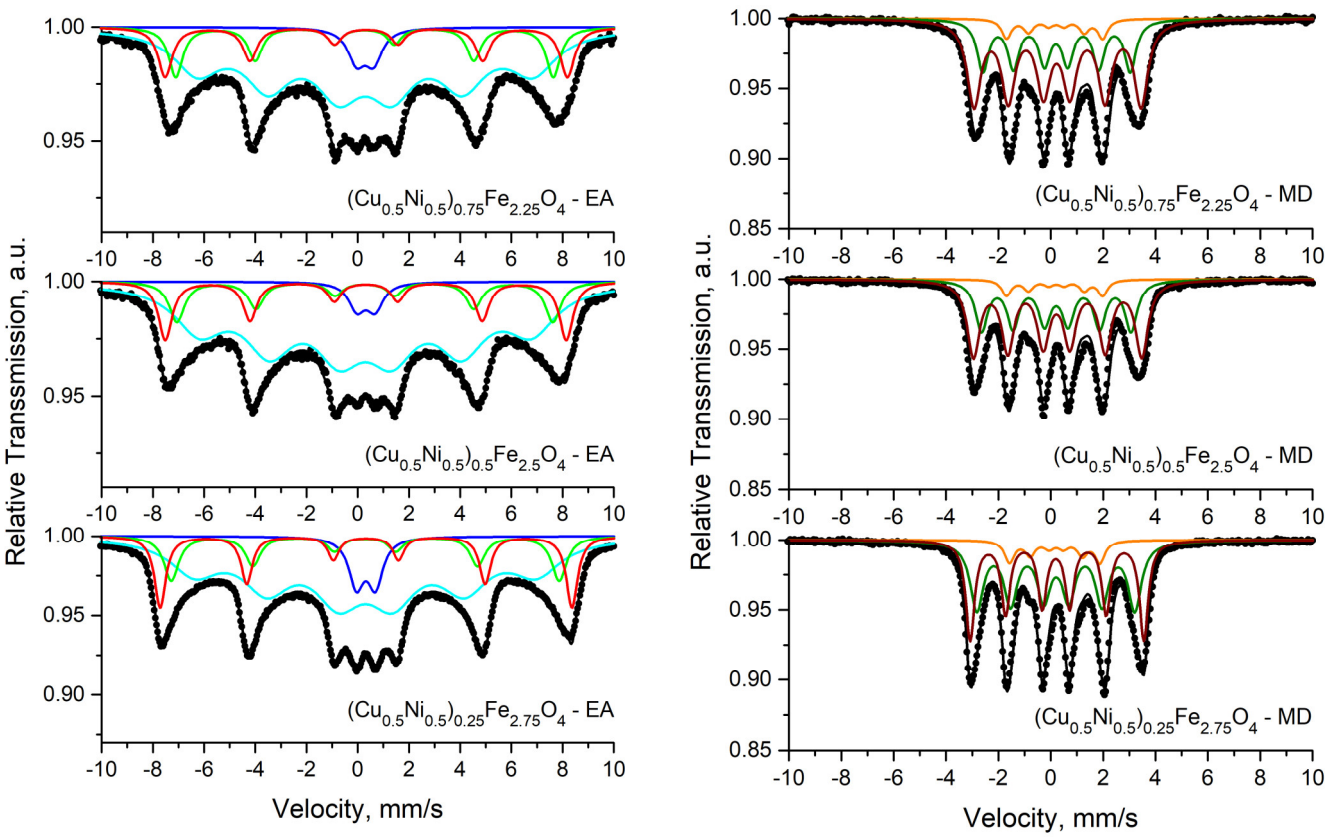

(**a**) (**b**)

Figure 7. Mössbauer spectra of the samples after catalyst test in the oxidation of ethyl acetate (**a**) and methanol decomposition (**b**).

Table 5. Mössbauer parameters of the samples after catalytic test in the oxidation of ethyl acetate and methanol decomposition.

Sample	Components	δ, mm/s	Δ (2ε), mm/s	B_{hf}, T	Γ_{exp}, mm/s	G, %
$(Cu_{0.5}Ni_{0.5})_{0.75}Fe_{2.25}O_4$-EA	Sx1-Fe^{3+}_{octa}	0.34	−0.01	48.7	0.67	14
	Sx2-Fe^{3+}_{tetra}	0.27	0.00	45.7	0.67	14
	Sx3-Fe^{3+}	0.29	0.00	40.7	2.22	67
	Db-Fe^{3+}	0.28	0.67	-	0.82	5
$(Cu_{0.5}Ni_{0.5})_{0.5}Fe_{2.5}O_4$-EA	Sx1-Fe^{3+}_{octa}	0.32	−0.01	48.5	0.65	14
	Sx2-Fe^{3+}_{tetra}	0.28	0.00	45.5	0.73	11
	Sx3-Fe^{3+}	0.30	0.00	40.2	2.35	71
	Db-Fe^{3+}	0.32	0.71	-	0.78	4
$(Cu_{0.5}Ni_{0.5})_{0.25}Fe_{2.75}O_4$-EA	Sx1-Fe^{3+}_{octa}	0.32	0.00	49.9	0.53	16
	Sx2-Fe^{3+}_{tetra}	0.29	0.00	47.0	0.70	13
	Sx3-Fe^{3+}	0.31	0.00	41.4	2.31	64
	Db-Fe^{3+}	0.32	0.75	-	0.72	7
$(Cu_{0.5}Ni_{0.5})_{0.75}Fe_{2.25}O_4$-MD	Sx1-χ-Fe_5C_2	0.24	0.03	19.8	0.63	61
	Sx2-χ-Fe_5C_2	0.21	0.02	17.5	0.53	32
	Sx3-χ-Fe_5C_2	0.18	−0.06	11.4	0.45	7
$(Cu_{0.5}Ni_{0.5})_{0.5}Fe_{2.5}O_4$-MD	Sx1-χ-Fe_5C_2	0.24	0.04	19.9	0.59	56
	Sx2-χ-Fe_5C_2	0.21	0.00	17.7	0.57	37
	Sx3-χ-Fe_5C_2	0.18	−0.07	11.4	0.45	7
$(Cu_{0.5}Ni_{0.5})_{0.25}Fe_{2.75}O_4$-MD	Sx1-χ-Fe_5C_2	0.21	0.04	20.6	0.40	42
	Sx2-χ-Fe_5C_2	0.20	−0.02	18.7	0.62	49
	Sx3-χ-Fe_5C_2	0.18	−0.06	10.7	0.45	9

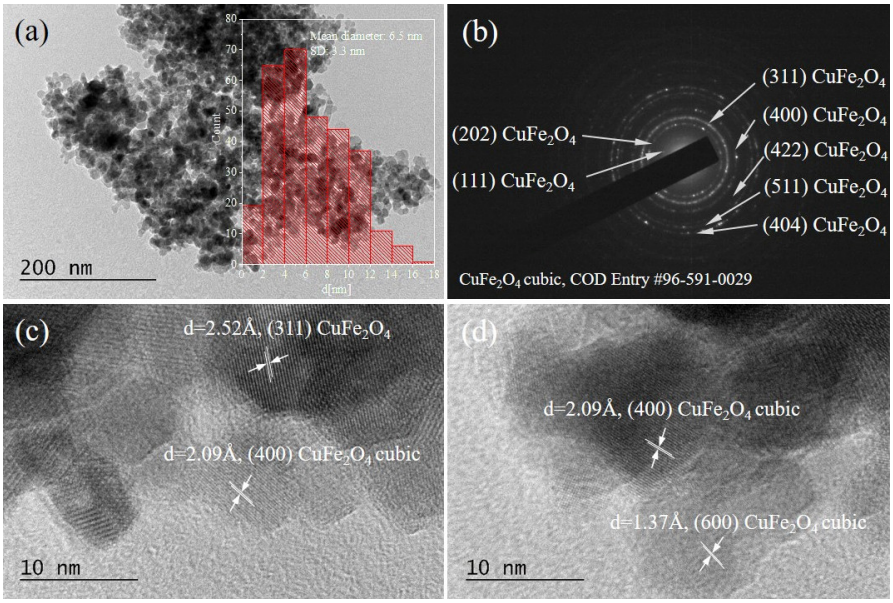

Figure 8. BFTEM micrograph and the particle size distribution histogram (**a**), the corresponding SAED pattern (**b**), and HRTEM micrographs (**c**,**d**) of $(Cu_{0.5}Ni_{0.5})_{0.5}Fe_{2.5}O_4$-EA, the catalytic material after a catalytic test for ethyl acetate.

The nitrogen physisorption data indicate that the observed differences in the catalytic behavior of the samples are not strongly related to their texture characteristics. Moreover, the XPS analyses demonstrated higher exposure of copper and nickel ions to the surface when compared to the expected theoretic one. Following the Mössbauer analyses, this could be assigned to the predominant location of metal ions on the most exposed octahedral

positions in the spinel lattice. In line with [36,37], these metal ions control the catalytic behavior of the samples. Despite the absence of phase transformations during the catalytic test, a significant agglomeration of the finely dispersed, and probably, most active, ferrite particles were distinctly observed by Mössbauer spectroscopy and HRTEM analyses. Obviously, with the increase in the (Cu + Ni)/Fe ratio, the increase in the ferrite dispersion combined with the increase in the portion of the Cu^{2+} and Ni^{2+} ions more exposed to the reactants, octahedral sites promote catalytic activity. However, the latter is suppressed by the simultaneous fast aggregation of the ferrite particles. Thus, the catalytic behavior of the samples was optimized for the $(Cu_{0.5}Ni_{0.5})_{0.5}Fe_{2.5}O_4$ sample.

Methanol decomposition was initiated above 500–520 K for all materials, and it exceeded about 100% conversion at 650 K (Figure 9). Within the whole temperature interval, the catalytic activity was the highest for $(Cu_{0.5}Ni_{0.5})_{0.25}Fe_{2.75}O_4$, and it decreased with the increase in Cu and Ni content in the samples. The conversion curves were characterized by changes in the slope or even the appearance of a maximum within the range of 550–575 K followed by a steep increase in the conversion above 600–650 K. These features were more pronounced and shifted to lower temperatures with the increase in the (Cu-Ni)/Fe ratio in the samples. The selectivity to CO was about 90%, and up to 3% and 7% methane and CO_2, respectively, were registered as by-products.

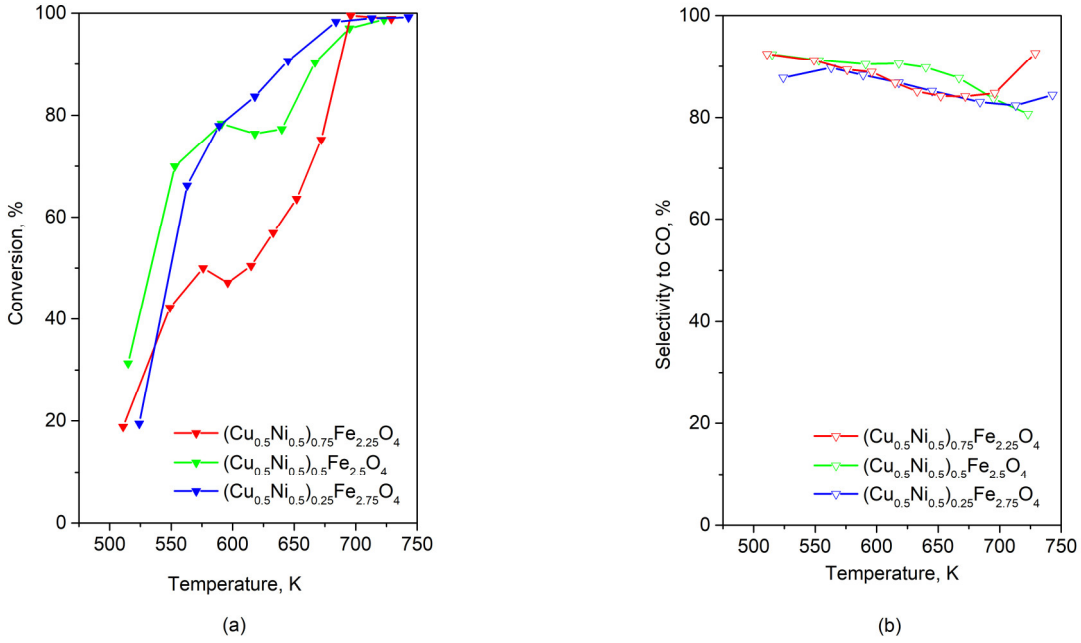

Figure 9. Conversion (**a**) and CO selectivity (**b**) vs. temperature in methanol decomposition for various samples.

The Mössbauer spectra of the samples after the reaction of methanol decomposition are presented in Figure 7b. The spectra are fitted using a model consisting of three sextets. The calculated Mössbauer parameters are summarized in Table 5. The parameters of the three sextets correspond to the three iron positions in Hägg carbide, χ-Fe_5C_2 [38,39].

TEM analysis of $(Cu_{0.5}Ni_{0.5})_{0.5}Fe_{2.5}O_4$-MD sample (Figure 10) confirms a significant change in morphology and phase composition in the sample after the catalytic test of methanol decomposition. As seen, the particles look embedded into envelopes, and they have much larger sizes as the mean diameter increased to 19.5 nm. SAED images are indexed with monoclinic Hägg carbide (monoclinic, a = 11.58800 Å b = 4.57900 Å c = 5.05900 Å, COD Entry #96-152-1832) and cubic $CuFe_2O_4$ (COD Entry #96-591-0029), but it is difficult to find the diffraction rings of the ferrite, which do not overlap with those of carbide. However, in HRTEM images (Figure 10), interplanar distances of cubic spinel ferrite d = 2.09 Å and d = 1.92 Å, corresponding to (400) and (313) crystal planes, are

visualized. The number of untransformed ferrite particles in the sample after methanol decomposition is probably very low because Mössbauer spectroscopy did not register any components related to ferrite. The Mössbauer study after the catalytic test indicated significant reduction transformations of the catalysts. Under the reaction medium, the spinel phase decomposed with the formation of Hägg carbide, and most probably, metallic copper and Ni. Considering the HRTEM study, the aggregation of the produced metal phases is assumed. Obviously, higher amounts of Cu and Ni in the samples promote the formation of less active Cu and Ni aggregates and Hägg carbide, which explains the observed complex.

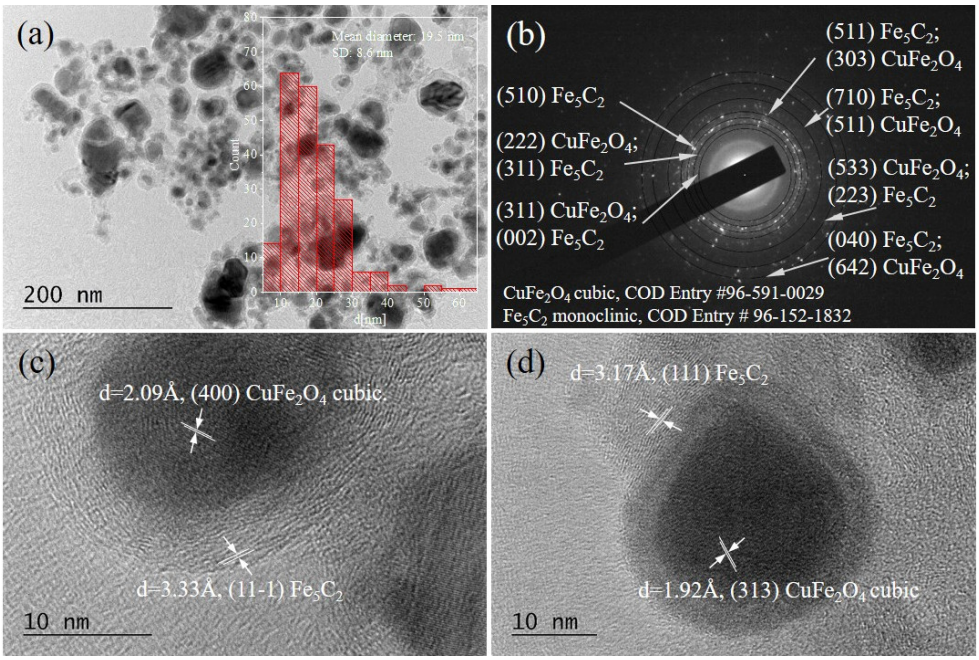

Figure 10. BFTEM micrograph and the particles size distribution histogram (**a**), the corresponding SAED pattern (**b**), and HRTEM micrographs (**c**,**d**) of $(Cu_{0.5}Ni_{0.5})_{0.5}Fe_{2.5}O_4$-MD, the catalytic material after a catalytic test for methanol decomposition.

4. Conclusions

Nanocrystalline materials with the composition $(Cu_{0.5}Ni_{0.5})_yFe_{3-y}O_4$, where y = 0.25, 0.5, and 0.75, were synthesized using the auto-combustion sol–gel method. A single cubic spinel phase was established in all samples. Decreasing the unit cell parameter and increasing the crystallite size with the decrease in copper and nickel content in ferrite compositions was evidenced by XRD analysis. TEM showed that synthesized ferrite materials consisted of particles with narrow size distributions. The main part of the particles in the sample $(Cu_{0.5}Ni_{0.5})_{0.5}Fe_{2.5}O_4$ has a size below 10 nm, and the mean diameter was calculated to be 4.3 nm. Mössbauer analysis determined that all iron ions are in the 3+ states. Thus, the cation distribution in the spinel structure of the compositions was proposed. The oxidation of EA was observed to be above 550–600 K. The conversion and the CO_2 selectivity increased with the temperature, and this effect was most pronounced for $(Cu_{0.5}Ni_{0.5})_{0.5}Fe_{2.5}O_4$. Analysis of samples after the catalytic activity test for ethyl acetate confirms the preservation of the cubic spinel structure and proves the recrystallization of ferrite particles as a result of heating up to 700 K during catalytic testing. Methanol decomposition was initiated above 500–520 K for all materials, and it reached about 100% conversion at 650 K. Within the whole temperature interval, the catalytic activity was the highest for $(Cu_{0.5}Ni_{0.5})_{0.25}Fe_{2.75}O_4$, and it decreased with the increase in Cu and Ni content in the samples. The analysis of samples after the catalytic test indicated significant reduction transformations inside the catalysts. Under the reaction medium, the spinel phase decomposed with the formation of Hägg carbide, which is evidenced by Mössbauer

spectroscopy and the HRTEM study of $(Cu_{0.5}Ni_{0.5})_{0.5}Fe_{2.5}O_4$. Also, the particles appeared embedded inside amorphous envelopes, and the mean diameter increased to 19.5 nm as they have much larger sizes.

Author Contributions: Conceptualization, N.V. and T.P.; methodology, N.V.; investigation, N.V., T.P., D.K. (Daniela Karashanova), G.A. and D.K. (Daniela Kovacheva); writing—original draft preparation, N.V.; writing—review and editing, D.K. (Daniela Karashanova); visualization, N.V. and T.P. All authors have read and agreed to the published version of the manuscript.

Funding: This research was funded by the Bulgarian Scientific Fund Project KP-06-H 29/2.

Data Availability Statement: Data are contained within the article.

Acknowledgments: The authors wish to express their sincere gratitude to Tanya Tsoncheva for conducting the catalytic tests of the materials and contributing to helpful discussions. Research equipment of the Distributed Research Infrastructure INFRAMAT, part of the Bulgarian National Roadmap for Research Infrastructures, supported by the Bulgarian Ministry of Education and Science, was used in this investigation.

Conflicts of Interest: The authors declare no conflicts of interest.

References

1. Narang, S.B.; Pubby, K. Nickel Spinel Ferrites: A review. *J. Magn. Magn. Mater.* **2021**, *519*, 167163. [CrossRef]
2. Pham, T.N.; Huy, T.Q.; Le, A.-T. Spinel ferrite (AFe_2O_4)-based heterostructured designs for lithium-ion battery, environmental monitoring, and biomedical applications. *RSC Adv.* **2020**, *10*, 31622–31661. [CrossRef]
3. Hao, A.; Ning, X. Recent Advances in Spinel Ferrite-Based Thin Films: Synthesis, Performances, Applications, and Beyond. *Front. Mater.* **2021**, *8*, 718869. [CrossRef]
4. Amiri, M.; Salavati-Niasari, M.; Akbari, A. Magnetic nanocarriers: Evolution of spinel ferrites for medical applications. *Adv. Colloid Interface Sci.* **2019**, *265*, 29–44. [CrossRef] [PubMed]
5. Maksoud, M.I.A.A.; Ghobashy, M.M.; Kodous, A.S.; Fahim, R.A.; Osman, A.I.; Al-Muhtaseb, A.H.; Rooney, D.W.; Mamdouh, M.A.; Nady, N.; Ashour, A.H. Insights on magnetic spinel ferrites for targeted drug delivery and hyperthermia applications. *Nanotechnol. Rev.* **2022**, *11*, 372–413. [CrossRef]
6. Kefeni, K.K.; Msagati, T.A.M.; Nkambule, T.T.; Mamba, B.B. Spinel ferrite nanoparticles and nanocomposites for biomedical applications and their toxicity. *Mater. Sci. Eng. C* **2020**, *107*, 110314. [CrossRef]
7. Soufi, A.; Hajjaoui, H.; Elmoubarki, R.; Abdennouri, M.; Qourzal, S.; Barka, N. Spinel ferrites nanoparticles: Synthesis methods and application in heterogeneous Fenton oxidation of organic pollutants—A review. *Appl. Surf. Sci. Adv.* **2021**, *6*, 100145. [CrossRef]
8. Qin, H.; He, Y.; Xu, P.; Huang, D.; Wang, Z.; Wang, H.; Wang, Z.; Zhao, Y.; Tian, Q.; Wang, C. Spinel ferrites (MFe2O4): Synthesis, improvement and catalytic application in environment and energy field. *Adv. Colloid Interface Sci.* **2021**, *294*, 102486. [CrossRef]
9. Peng, Y.; Tang, H.; Yao, B.; Gao, X.; Yang, X.; Zhou, Y. Activation of peroxymonosulfate (PMS) by spinel ferrite and their composites in degradation of organic pollutants: A Review. *J. Chem. Eng.* **2021**, *414*, 128800. [CrossRef]
10. Pund, S.N.; Nagwade, P.A.; Nagawade, A.V.; Thopate, S.R.; Bagade, A.V. Preparation techniques for zinc ferrites and their applications: A review. *Mater. Today Proc.* **2022**, *60*, 2194–2208. [CrossRef]
11. Velinov, N.; Petrova, T.; Genova, I.; Ivanov, I.; Tsoncheva, T.; Idakiev, V.; Kunev, B.; Mitov, I. Synthesis and Mössbauer spectroscopic investigation of copper-manganese ferrite catalysts for water-gas shift reaction and methanol decomposition. *Mater. Res. Bull.* **2017**, *95*, 556–562. [CrossRef]
12. Shamim, K.; Sharma, S.; Choudhary, R.J. Role of ferrite phase on the structure, dielectric and magnetic properties of (1-x) KNNL/x NFO composites ceramics. *J. Magn. Magn. Mater.* **2019**, *469*, 1–7. [CrossRef]
13. Qin, X.; Zhang, T.; Wang, J.; Zhao, R.; Ma, Y.; Wang, F.; Xu, X. Influence of Ce-Mn co-doping on the structure and magnetic properties of cobalt ferrites. *J. Alloys Compd.* **2022**, *929*, 167256. [CrossRef]
14. Goud, S.; Venkatesh, N.; Kumar, D.R.; Barapati, S.; Veerasomaiah, P. Study of structural, optical, photocatalytic, electromagnetic, and biological properties $Co_{0.75}Mg_{0.25}Ce_xFe_{2-x}O_4$ of Mg-Co nano ferrites. *Inorg. Chem. Commun.* **2022**, *145*, 109969. [CrossRef]
15. Noreen, S.; Hussain, A.; Tahir, M.B.; Ziya, A.B.; Rehman, J.U.; Usman, M.; Khan, S.A.; Akhtar, S. Structural, mechanical, thermodynamic, electronic, magnetic and optical properties of $ZnFe_2O_4$ ferrite: A DFT study. *Opt. Mater.* **2022**, *133*, 112930. [CrossRef]
16. Baig, N.; Kammakakam, I.; Falath, W. Nanomaterials: A review of synthesis methods, properties, recent progress, and challenges. *Mater. Adv.* **2021**, *2*, 1821–1871. [CrossRef]
17. Ivanova, I.V.; Zaitseva, N.A.; Samigullina, R.F.; Krasnenko, T.I. Solid-state synthesis of $ZnMn_2O_4$ spinel: Sequence of phase transformations, thermal stability, localization and charge state of manganese ions in the intermediate and final reaction products. *Solid State Sci.* **2023**, *136*, 107110. [CrossRef]

18. Velinov, N.; Koleva, K.; Tsoncheva, T.; Manova, E.; Paneva, D.; Tenchev, K.; Kunev, B.; Mitov, I. Nanosized $Cu_{0.5}Co_{0.5}Fe_2O_4$ ferrite as catalyst for methanol decomposition: Effect of preparation procedure. *Catal. Commun.* **2012**, *32*, 41–46. [CrossRef]
19. Velinov, N.; Manova, E.; Tsoncheva, T.; Estournès, C.; Paneva, D.; Tenchev, K.; Petkova, V.; Koleva, K.; Kunev, B.; Mitov, I. Spark plasma sintering synthesis of $Ni_{1-x}Zn_xFe_2O_4$ ferrites: Mössbauer and catalytic study. *Solid State Sci.* **2012**, *14*, 1092–1099. [CrossRef]
20. Velinov, N.; Koleva, K.; Tsoncheva, T.; Paneva, D.; Manova, E.; Tenchev, K.; Kunev, B.; Genova, I.; Mitov, I. Copper-cobalt ferrites as catalysts for methanol decomposition. *Cent. Eur. J. Chem.* **2014**, *12*, 250–259. [CrossRef]
21. Varma, A.; Mukasyan, A.S.; Rogachev, A.S.; Manukyan, K.V. Solution Combustion Synthesis of Nanoscale Materials. *Chem. Rev.* **2016**, *116*, 14493–14586. [CrossRef]
22. Lazarova, T.; Georgieva, M.; Tzankov, D.; Voykova, D.; Aleksandrov, L.; Cherkezova-Zheleva, Z.; Kovacheva, D. Influence of the type of fuel used for the solution combustion synthesis on the structure, morphology and magnetic properties of nanosized $NiFe_2O_4$. *J. Alloys Comp.* **2017**, *700*, 272–283. [CrossRef]
23. Lazarova, T.; Kovacheva, D.; Georgieva, M.; Tzankov, D.; Tyuliev, G.; Spassova, I.; Naydenov, A. Tunable nanosized spinel manganese ferrites synthesized by solution combustion method. *Appl. Surf. Sci.* **2019**, *496*, 143571. [CrossRef]
24. Perez-Hernandez, R.; Avendano, A.D.; Rosas, E.; Rodrıguez, V. Hydrogen Production by Methanol Steam Reforming Over Pd/ZrO_2–TiO_2 Catalysts. *Top. Catal.* **2011**, *54*, 572–578. [CrossRef]
25. López, P.; Mondragón-Galicia, G.; Espinosa-Pesqueira, M.E.; Mendoza-Anaya, D.; Fernández, M.E.; Gómez-Cortés, A.; Bonifacio, J.; Martínez-Barrera, G.; Pérez-Hernández, R. Hydrogen production from oxidative steam reforming of methanol: Effect of the Cu and Ni impregnation on ZrO_2 and their molecular simulation studies. *Int. J. Hydrogen Energy* **2012**, *37*, 9018–9027. [CrossRef]
26. Zhou, Y.; Zhang, H.; Yan, Y. Catalytic oxidation of ethyl acetate over CuO/ZSM-5 catalysts: Effect of preparation method. *J. Taiwan Inst. Chem. Eng.* **2018**, *84*, 162–172. [CrossRef]
27. Qin, Y.; Shen, F.; Zhu, T.; Honga, W.; Liu, X. Catalytic oxidation of ethyl acetate over $LaBO_3$ (B=Co, Mn, Ni, Fe) perovskites supported silver catalysts. *RSC Adv.* **2018**, *8*, 33425. [CrossRef]
28. Cornell, R.M.; Schwertmann, U. *The Iron Oxides: Structure, Properties, Reactions, Occurrences and Uses*; Wiley-VCH Verlag GmbH & Co. KGaA: Hoboken, NJ, USA, 2003; pp. 1–664. [CrossRef]
29. Kalska-Szostko, B.; Wykowska, U.; Satula, D.; Nordblad, P. Thermal treatment of magnetite nanoparticles. *Beilstein J. Nanotechnol.* **2015**, *6*, 1385–1396. [CrossRef] [PubMed]
30. Biesinger, M.C. Advanced analysis of copper X-ray photoelectron spectra. *Surf. Interface Anal.* **2017**, *49*, 1325–1334. [CrossRef]
31. Biesinger, M.C.; Payne, B.P.; Lau, L.W.M.; Gerson, A.; Smart, R.S.C. X-ray photoelectron spectroscopic chemical state quantification of mixed nickel metal, oxide and hydroxide systems. *Surf. Interface Anal.* **2009**, *41*, 324–332. [CrossRef]
32. Yamashita, T.; Hayes, P. Analysis of XPS spectra of Fe^{2+} and Fe^{3+} ions in oxide materials. *Appl. Surf. Sci.* **2008**, *254*, 2441–2449. [CrossRef]
33. Biesinger, M.C.; Payne, B.P.; Grosvenor, A.P.; Lau, L.W.M.; Gerson, A.R.; Smart, R.S.C. Resolving surface chemical states in XPS analysis of first row transition metals, oxides and hydroxides: Cr, Mn, Fe, Co and Ni. *Appl. Surf. Sci.* **2011**, *257*, 2717–2730. [CrossRef]
34. Sing, K.S.W.; Everett, D.H.; Haul, R.A.W.; Moscou, L.; Pierotti, R.A.; Rouquerol, J.; Siemieniewska, T. Reporting physisorption data for gas/solid systems with special reference to the determination of surface area and porosity. *Pure Appl. Chem.* **1985**, *57*, 603–619. [CrossRef]
35. ALOthman, Z.A. A Review: Fundamental Aspects of Silicate Mesoporous Materials. *Materials* **2012**, *5*, 2874–2902. [CrossRef]
36. Jacobs, J.P.; Maltha, A.; Reintjes, J.G.H.; Drimal, J.; Ponec, V.; Brongersma, H.H. The Surface of Catalytically Active Spinels. *J. Catal.* **1994**, *147*, 294–300. [CrossRef]
37. El-Shobaky, H.G.; Mokhtar, M.M. Effect of Li_2O and CoO-doping of CuO/Fe_2O_3 system on its surface and catalytic properties. *Appl. Surf. Sci.* **2007**, *253*, 9407–9413. [CrossRef]
38. Liu, X.-W.; Zhao, S.; Meng, Y.; Peng, Q.; Dearden, A.K.; Huo, C.-F.; Yang, Y.; Li, Y.-W.; Wen, X.-D. Mössbauer spectroscopy of iron carbides: From prediction to experimental confirmation. *Sci. Rep.* **2016**, *6*, 26184. [CrossRef]
39. Velinov, N.; Petrova, T.; Tsoncheva, T.; Genova, I.; Koleva, K.; Kovacheva, D.; Mitov, I. Auto-combustion synthesis, Mössbauer study and catalytic properties of copper-manganese ferrites. *Hyperfine Interact.* **2016**, *237*, 24. [CrossRef]